Analytica Chimica Acta 1200 (2022) 339609

Contents lists available at ScienceDirect

Analytica Chimica Acta

journal homepage: www.elsevier.com/locate/aca

Electrochemical neuron-specific enolase (NSE) immunosensor based on $CoFe_2O_4$@Ag nanocomposite and AuNPs@MoS_2/rGO

Ceren Karaman [a], Ömer Saltuk Bölükbaşı [b], Bahar Bankoğlu Yola [c], Onur Karaman [d], Necip Atar [e], Mehmet Lütfi Yola [f, *]

[a] Akdeniz University, Vocational School of Technical Sciences, Department of Electricity and Energy, Antalya, Turkey
[b] Iskenderun Technical University, Faculty of Engineering and Natural Sciences, Department of Metallurgical and Materials Engineering, Hatay, Turkey
[c] Iskenderun Technical University, Science and Technology Application and Research Laboratory, Hatay, Turkey
[d] Akdeniz University, Vocational School of Health Services, Department of Medical Imaging Techniques, Antalya, Turkey
[e] Pamukkale University, Faculty of Engineering, Department of Chemical Engineering, Denizli, Turkey
[f] Hasan Kalyoncu University, Faculty of Health Sciences, Department of Nutrition and Dietetics, Gaziantep, Turkey

HIGHLIGHTS

- Electrochemical immunosensor is developed for small cell lung cancer disease detection.
- The prepared electrochemical immunosensor is characterized by several methods.
- The excellent reliability for the protocol of immunosensor fabrication is presented.
- This assay is advantageous in comparison with the other analytical methods.

GRAPHICAL ABSTRACT

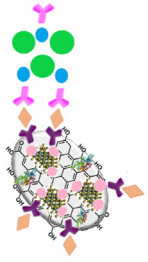

Electrochemical neuron-specific enolase (NSE) immunosensor

ARTICLE INFO

Article history:
Received 13 January 2022
Received in revised form
2 February 2022
Accepted 14 February 2022
Available online 16 February 2022

Keywords:
Neuron-specific enolase
Diagnosis
Voltammetry
Nanocomposite
Immunosensor

ABSTRACT

Small cell lung cancer (SCLC) is highly associated with the risk of early metastasis. Neuron-specific enolase (NSE), a biomarker of SCLC, is directly related to tumor burden and early diagnosis. This biomarker exists in nerve tissue and neuroendocrine tissue. In this study, an electrochemical NSE immunosensor based on gold nanoparticles modified molybdenum disulfide and reduced graphene oxide (AuNPs@MoS_2/rGO) as the electrode platform and $CoFe_2O_4$@Ag nanocomposite as the signal amplification was developed. The immobilization of anti-NSE capture antibody was successfully performed on AuNPs@MoS_2/rGO modified electrode surface by amino-gold affinity and the conjugation of anti-NSE secondary antibody on $CoFe_2O_4$@Ag nanocomposite was successfully completed by the strong esterification reaction. The final immunosensor was designed by the specific interactions of electrode platform and signal amplification. The fabricated nanocomposites and electrochemical immunosensor were characterized by both physicochemical characterization techniques including transmission electron microscopy (TEM), scanning electron microscopy (SEM), x-ray diffraction (XRD), x-ray photoelectron spectroscopy (XPS), fourier transform infrared spectroscopy (FTIR), and electrochemical methods such as cyclic voltammetry (CV), square wave voltammetry (SWV), and electrochemical impedance spectroscopy (EIS). The quantification limit (LOQ) and the determination limit (LOD) were computed to be 0.01 pg mL^{-1} and 3.00 fg mL^{-1}, respectively. In brief, it can be speculated that the constructed electrochemical NSE immunosensor can be successfully utilized in the early diagnosis for lung cancer.

* Corresponding author.
E-mail address: mlutfi.yola@hku.edu.tr (M.L. Yola).

https://doi.org/10.1016/j.aca.2022.339609
0003-2670/

1. Introduction

Small cell lung cancer, a histological subgroup of lung cancer, has an inadequate prognosis, a high rate of metastasis, and a high percentage of proliferative rate, and is frequently diagnosed in the middle to late stages of the disease [1,2]. Moreover, SCLC accounting for approximately 20% of lung cancer cases is a disease that is difficult to treat and has a low survival rate even after aggressive treatment methods [3]. As a result, developing high-sensitivity early determination technologies is critical to preventing metastasis and lowering the fatality rate. The level in the blood of neuron-specific enolase (NSE), which is detectable in both nerve and neuroendocrine tissues [4], is around 10–12 ng mL^{-1} in healthy people and is correlated to the clinical manifestations of SCLC [5,6]. Hence, it can be concluded that the development of a highly sensitive approach with a broader linear determination range for the quantitative monitoring of NSE in serum is crucial. Up till now, many approaches have been reported for the determination of distinct biomarkers, including enzyme-linked immunosorbent assay, radioimmunoassay, fluorescence immunoassay, and chemiluminescence immunoassay [7–9]. However, compared to these proposed methods, electrochemical immunosensors, which transform immunological responses triggered by specific probe-target complexes into legible current signals, have garnered substantial attention thanks to their peculiar features including ease-of-use, being portable, cost-effectiveness, and superior sensitivity [10,11]. The most common and effective method applied to boost the sensitivity of electrochemical immunosensors is the signal amplification approach [12]. In this context, two distinct approaches can be followed both to increase the current signal by using a label with high catalytic activity and to facilitate the electron transport efficiency of the substrate by preserving the activity of the immune molecule [13,14]. Several types of nanomaterials such as carbon-based nanoarchitectures, quantum dots, metal nanoparticles, etc. have been used in diverse application fields thanks to state-of-the-art breakthroughs in nanotechnology [15–19], and signal amplification for boosted electrochemical immunosensing is also one of them.

The nanocomposites based on graphene/graphene oxide (GO) and MoS_2 have started to get significant attention owing to the physical and chemical features [20,21]. Especially, GO can be converted to rGO to improve the conductivity by eliminating oxygenated species and preventing unwanted electrochemical reactions [22]. In addition, Graphene and MoS_2 nanocomposites with metal nanoparticles can improve the rate of electron transport, resulting in high sensitivity [23,24]. For instance, AuNPs@MoS_2/rGO nanocomposite was fabricated by the hydrothermal and chemical reduction techniques for nitrite determination, and the LOD of 0.038 μM was achieved [25]. While a considerable focus has been paid on the graphene/graphene oxide and MoS_2 nanostructures, several studies on AuNPs@MoS_2/rGO as an electrode platform have been also presented.

Fe_3O_4NPs have high surface area, good superparamagnetism, low toxicity, and easy preparation [26]. In recent years, the nanostructures based on magnetic Fe_3O_4NPs have been employed in various biomedical applications such as magnetic isolation [27,28], and biosensor/nanosensor fabrication [29,30]. For instance, the strong interaction between Fe_3O_4 and hemoglobin could cause low purity cell separation [27]. Moreover, due to the strong interactions between Co and Fe metals in $CoFe_2O_4$ nanomaterials, high coercivity, and anisotropy properties, $CoFe_2O_4$ nanostructures can also offer enhanced magnetic properties with keeping iron oxides' inherent features. Moreover, $CoFe_2O_4$ nanostructures have high magneto-crystalline anisotropy, good magnetization strength, chemical stability, and colloidal dispersibility, thereby providing the improvement of magnetic separation's quality [27]. Especially, the preparations of $CoFe_2O_4$ and their composites are of great significance in biosensor applications due to their high biocompatibility and physicochemical features. Until now, several unique $CoFe_2O_4$ based nanocomposites have been reported such as Zn^{2+}/silica-modified $CoFe_2O_4$ [31], $CoFe_2O_4$ including chitosan [32], and $CoFe_2O_4$ including gold nanoparticles [33] for the pollutants' separation. Nonetheless, $CoFe_2O_4$ based nanocomposites have been generally produced via costly and time-consuming techniques. Thus, green approaches with minimal material utilization are highly necessary to prepare multifunctional $CoFe_2O_4$ based nanocomposites. The conductive nanostructures play a significant function for enhancing the performance of electrochemical platforms by allowing for larger specific electroactive areas. As a result, a large number of binding sites towards specific proteins can be generated, providing selective recognition in complicated matrix samples.

Herein, bearing all the aforementioned points in mind, an electrochemical neuron-specific enolase immunosensor based on $CoFe_2O_4$@Ag nanocomposite and AuNPs@MoS_2/rGO was proposed for the first time in literature. The prepared electrochemical neuron-specific enolase immunosensor illustrated several major benefits including superior selectivity without interference in plasma samples, sensitivity with LOD of 3.00 fg mL^{-1}, ease of use, and health and environmental compliance. Hence, this work paves the way for engineering highly selective and sensitive electrochemical neuron-specific enolase immunosensor to be utilized in the early diagnosis of small cell lung cancer by monitoring NSE.

2. Experimental

2.1. Materials

Neuron-specific enolase (NSE), anti-NSE capture antibody (anti-NSE-Ab_1), anti-NSE secondary antibody (anti-NSE-Ab_2), bovine serum albumin (BSA), prostate specific antigen (PSA), carcinoembryonic antigen (CEA), cardiac troponin I (cTnI), graphite, potassium permanganate ($KMnO_4$), hydrogen peroxide (H_2O_2), Na_2MoO_4 $2H_2O$, thiourea (CH_4N_2S), gold(III) chloride ($HAuCl_4$), $Co(NO_3)_2 \cdot 6H_2O$, $Fe(NO_3)_3 \cdot 9H_2O$, $AgNO_3$, sodium citrate ($Na_3C_6H_5O_7$), 1-ethyl-3-carbodiimide hydrochloride (EDC) and N-hydroxysuccinimide (NHS) were supplied from Sigma-Aldrich. 0.1 M phosphate-buffered saline (PBS) solution with a pH value of 7.0 was selected to serve as both a supporting electrolyte and dilution buffer solution.

2.2. Physicochemical and electrochemical characterization techniques

ZEISS EVO 50 SEM (Carl-Zeiss-Stiftung, Germany) and JEOL 2100 TEM (JEOL Ltd., Tokyo, Japan) were employed to examine the surface morphologies of nanostructures. The XRD spectra of the nanomaterials were collected using a Rigaku X-ray diffractometer (MiniFlex, Japan/USA) with Cu-Kα radiation at a wavelength of 0.154 nm, and XPS analysis was performed using a PHI 5000 Versa Probe type x-ray photoelectron spectrometer (Φ ULVAC-PHI.Inc., Japan/USA). Additionally, for electrochemical characterizations of the constructed electrodes, the Gamry Reference 600 work-station (Gamry, USA) was used to conduct CV, EIS, and SWV investigations.

2.3. Synthesis of rGO, MoS_2/rGO and AuNPs@MoS_2/rGO

rGO synthesis was performed according to our previously reported study [34]. Briefly, the mixture of $NaNO_3$ (2.0 g) and graphite (4.0 g) was firstly prepared. Afterward, the dispersion was stirred at

4 °C following the introduction of H_2SO_4 (98%, 200.0 mL) into the mixture. At the end of 30 min, $KMnO_4$ (4.5 g) was added into this dispersion. The resultant dispersion was poured into H_2O_2 (30.0 mL, 30.0 wt%) solution and mixed at 25 °C for 45 min. The obtained nanomaterial was washed with HCl solution (20%) three times.

For ***MoS_2/rGO*** production, the Na_2MoO_4 $2H_2O$ (10.0 mg) and CH_4N_2S was mixed with rGO suspension (1.0 mg mL^{-1}, 20.0 mL), and dispersed under vigorous stirring. Subsequently, the dispersion was subjected to thermal treatment at 210 °C over 20 h in an autoclave reactor. The resultant product was washed with ultra pure water three times.

AuNPs@MoS_2/rGO synthesis was performed via a facile reduction approach at 25 °C. Following the addition of $HAuCl_4$ (2.0 mg mL^{-1}, 10.0 mL) and lysine (5.0 mL) into the MoS_2/rGO solution (1.0 mg mL^{-1}, 10.0 mL) under strong stirring over 20 min, the cold sodium borohydride solution (0.01 mol L^{-1}, 1.0 mL) was gently added into the above solution over a period of 25 min. The resultant ***AuNPs@MoS_2/rGO*** structure was collected by centrifugation and washed with ultrapure water triple times.

2.4. AuNPs@MoS_2/rGO modified glassy carbon electrode as electrochemical sensor platform with anti-NSE-Ab_1 and antigen NSE immobilizations

Following the previously described cleaning technique, the glassy carbon electrode (GCE) with a geometric area of 0.027 cm^2 was kept ready for its upcoming use [35]. Alumina slurries of various particle sizes were deposited onto polishing pads, and GCE was shined with these alumina slurries over a 10 min period. Following the rinsing of GCE with acetonitrile at 25 °C to eliminate residual alumina on the GCE, AuNPs@MoS_2/rGO dispersion (20.0 μL, 0.2 mg mL^{-1}) was dropped onto the clean GCE surface. After 30 min, the solvent was removed by an infrared heat lamp, producing AuNPs@MoS_2/rGO modified GCEs (***AuNPs@MoS_2/rGO/GCE***). Finally, the same fabrication method was carried out to prepare rGO and MoS_2/rGO modified GCEs (***rGO/GCE*** and ***MoS_2/rGO/GCE)***.

20.0 μL of as-prepared anti-NSE-Ab_1 solution (20.0 μg mL^{-1}) was dropped on AuNPs@MoS_2/rGO/GCE, resulting ***anti-NSE-Ab_1/AuNPs@MoS_2/rGO/GCE*** via amino-gold affinity between primer anti-NSE-Ab_1 and AuNPs@MoS_2/rGO/GCE at 37.0 °C for 20 min. Then, BSA (2.0% w/v) was interacted with anti-NSE-Ab_1/AuNPs@MoS_2/rGO/GCE at 37.0 °C for 20 min to eliminate the non-specific interactions (***BSA/anti-NSE-Ab_1/AuNPs@MoS_2/rGO/GCE***). After the incubation of antigen NSE proteins having different concentration on BSA/anti-NSE-Ab_1/AuNPs@MoS_2/rGO/GCE, the final electrode (***NSE/BSA/anti-NSE-Ab_1/AuNPs@MoS_2/rGO/GCE***) was rinsed with 0.1 M PBS (pH 7.0) to eliminate non-contacted proteins.

2.5. Synthesis of $CoFe_2O_4$ and $CoFe_2O_4$@Ag nanocomposite as signal amplification and anti-NSE-Ab_2 conjugation

For preparation of $CoFe_2O_4$ nanostructure, $Co(NO_3)_2 \cdot 6H_2O$ (2.50 g) and $Fe(NO_3)_3 \cdot 9H_2O$ (7.00 g) were firstly dissolved in ultra pure water under strong stirring during 20 min. After that, the obtained dispersion was introduced into NaOH solution (30.0 mL, 2.0 mol L^{-1}). Following the thermal treatment at 120 °C for 20 h in an autoclave reactor, ***$CoFe_2O_4$*** was collected with the help of a magnet and washed with ultra pure water three times [31].

$CoFe_2O_4$ (0.250 g) and $AgNO_3$ (0.100 g) were mixed together in ultra pure water (150.0 mL) and the heating treatment was started. At the end of the period of 20 min, $Na_3C_6H_5O_7$ (15.0 mg mL^{-1}, 20.0 mL) was added into above solution under vigorous stirring. $Na_3C_6H_5O_7$ served as a stabilizer during the reduction of Ag^+ to metallic silver by controlling the growth of Ag nanoparticles, and also provided −COOH groups on $CoFe_2O_4$@Ag nanocomposite. The color shifted from dark brown to light brown after 20 min, indicating the ***$CoFe_2O_4$@Ag*** nanocomposite. This nanocomposite was centrifuged at 1000 rpm for 20 min and collected with a magnet, then dried at 50 °C [36,37].

After preparation of the anti-NSE-Ab_2 (20.0 μL, 20.0 μg mL^{-1}), anti-NSE-Ab_2 solution interacted with $CoFe_2O_4$@Ag nanocomposite via a strong esterification reaction between $-NH_2$ group of anti-NSE-Ab_2 and −COOH group of $CoFe_2O_4$@Ag nanocomposite at 37.0 °C for 20 min [38]. For this esterification reaction, 10.0 μL of EDC/NHS solution (20.0 mM/4.0 mM) was firstly added to $CoFe_2O_4$@Ag nanocomposite (10.0 μL, 2.0 mg mL^{-1}) to activate −COOH groups of $CoFe_2O_4$@Ag nanocomposite, and the obtained ***anti-NSE-Ab_2/$CoFe_2O_4$@Ag*** was stored in a 0.1 M PBS solution with pH = 7.0.

2.6. Assessment of the electrochemical performance of the fabricated immunosensor

The final electrochemical NSE immunosensor was fabricated by the associations between the NSE/BSA/anti-NSE-Ab_1/AuNPs@MoS_2/rGO/GCE and anti-NSE-Ab_2/$CoFe_2O_4$@Ag through the characteristic antibody-antigen interaction. anti-NSE-Ab_2/$CoFe_2O_4$@Ag (25.0 μL, 20.0 mg mL^{-1}) was incubated on NSE/BSA/anti-NSE-Ab_1/AuNPs@MoS_2/rGO/GCE for 25 min to provide this interaction. As a result, the final NSE immunosensor (***GCE/rGO/MoS_2@AuNPs/anti-NSE-Ab_1/BSA/NSE/anti-NSE-Ab_2/$CoFe_2O_4$@Ag***) was stored in pH 7.0, 0.1 M PBS (3.0 mL). During all electrochemical experiments, a typical three-electrode setup electrochemical cell was utilized. In this regard, Ag/AgCl (sat KCl), and Pt-wire electrodes were employed as the reference and the counter electrodes, respectively. Before the electrochemical experiments, to remove the dissolved O_2 molecules in the solution, it was saturated with the high purity Argon gas over 20 min.

2.7. Samples preparation strategy

The overall strategy for preparing the samples was described thoroughly on Supplementary Data [39].

3. Results and discussion

3.1. Fundamental of electrochemical immunosensor based on AuNPs@MoS_2/rGO and $CoFe_2O_4$@Ag nanocomposite

AuNPs@MoS_2/rGO nanocomposite as electrode platform was prepared by a facile reduction method in the presence of $HAuCl_4$. The incorporation of AuNPs into nanocomposite improved the surface conductivity for electrochemical sensitivity [40]. Afterward, the immobilization of anti-NSE-Ab_1 on the electrode platform was carried out by amino-gold affinity between primer anti-NSE-Ab_1 and AuNPs@MoS_2/rGO/GCE.

$CoFe_2O_4$@Ag nanocomposite as a signal amplification was prepared by a cost-effective and facile hydrothermal technique. The nanocomposite was functionalized with −COOH groups via sodium citrate where it served as a reducing agent for Ag^+. Thereafter, a stable anti-NSE-Ab_2/$CoFe_2O_4$@Ag nanocomposite was synthesized by a strong esterification reaction between anti-NSE-Ab_2 and $CoFe_2O_4$@Ag nanocomposite. Lastly, H_2O_2 solution (1.0 mM) as a redox probe was used due to its easy oxidation into O_2 and preferably availability in immunosensor technology [41,42]. Scheme 1 depicted a schematic representation of the electrochemical NSE immunosensor production approach based on the electrochemical reaction mechanism of $\boldsymbol{H_2O_2 \leftrightarrow O_2 + 2H^+ + 2e^-}$.

3.2. Characterizations of $CoFe_2O_4$@Ag nanocomposite

XRD spectra (Fig. S1A) depicted the crystal structure of $CoFe_2O_4$. The crystal planes including (111), (220), (311), (400), (422), (511), (440) and (533) indicated $CoFe_2O_4$'s cubic spinel structure [33,43]. The XRD peak corresponding to the (311) plane confirmed $CoFe_2O_4$'s good crystalline structure. The chemical structure of $CoFe_2O_4$@Ag nanocomposite was investigated by using FTIR (Fig. S1B) and UV–Vis spectroscopy (Fig. S1C). FTIR spectrum of $CoFe_2O_4$ demonstrated an obvious absorption band at *ca.*589 cm^{-1} relating to Co–O and Fe–O bounds whereas this absorption band shifted to 583 cm^{-1} on FTIR spectrum of $CoFe_2O_4$@Ag owing to the interaction of Ag nanoparticles with the octahedral lattice of $CoFe_2O_4$ [44]. In addition, the absorption bands corresponding to 1378 and 1569 cm^{-1} revealed the presence of stretching –COO– on FTIR spectrum of $CoFe_2O_4$@Ag nanocomposite [45]. Thus, FTIR spectra of $CoFe_2O_4$ and $CoFe_2O_4$@Ag nanocomposite affirmed the successful synthesis of $CoFe_2O_4$@Ag nanocomposite and the efficient functionalization of $CoFe_2O_4$@Ag with –COOH groups providing the binding sites towards NSE protein via esterification reaction. According to Fig. S1C, the absorption spectrum of $CoFe_2O_4$@Ag nanocomposite was different from that of $CoFe_2O_4$ owing to the incorporation of silver nanoparticles into nanocomposite. There was no obvious absorption band on UV–Vis spectrum of $CoFe_2O_4$ whereas the absorption band at about 425–431 nm was observed, indicating the presence of silver nanoparticles [46].

SEM images were obtained for the investigation of surface morphology and particle size features of $CoFe_2O_4$@Ag nanocomposite and $CoFe_2O_4$. $CoFe_2O_4$ nanospheres with a uniform size distribution were observed on Fig. 1A, providing an average diameter of 50–85 nm. In addition, $CoFe_2O_4$@Ag nanocomposite with an average diameter of 65–93 nm was detected on Fig. 1B. The elements' distribution including Co, Fe, O, Ag and C elements was depicted on the mapping analysis (Fig. S2), confirming a homogeneous distribution except for several silver aggregations. The presence of C element was also resulted from the introduction of citrate groups during the $CoFe_2O_4$@Ag nanocomposite fabrication step. Fig. S3 showed EDX image of (A) $CoFe_2O_4$, (B) $CoFe_2O_4$@Ag nanocomposite. According to Fig. S3, it was confirmed that the successful preparations of $CoFe_2O_4$ and $CoFe_2O_4$@Ag nanocomposite were achieved in this study.

The surface composition and the element valence of $CoFe_2O_4$@Ag nanocomposite were investigated by XPS (Fig. 2). The high-resolution XPS spectrum (Fig. 2A) of C1s, Fe2p, Co2p, O 1s, and Ag3d was in harmony with the results of EDX analysis. Two XPS peaks at 284.78 and 288.96 eV were corresponded to C–C and C–O bonds, respectively (Fig. 2B) [30]. For Fe2p high-resolution XPS spectrum (Fig. 2C), four peaks at 712.11 (Fe2p3/2), 714.23 (Fe2p1/2), 720.14 (Fe2p1/2) and 726.36 eV (Fe2p3/2) were observed [37]. The peaks at 712.16, and 726.33 eV were attributed to Fe^{3+} ions in the octahedral, and Fe^{3+} ions in tetrahedral sites, respectively [47]. According to Co2p high-resolution XPS spectrum (Fig. 2D), XPS peaks at 780.81, 790.17, 797.19 and 806.18 eV were detected. XPS peaks at 780.81 and 790.17 were corresponded to Co^{2+} ions in the octahedral and tetrahedral sites, respectively [37]. For high-resolution XPS spectrum of the O1s orbital(Fig. 2E), the peaks observed at 530.17 and 531.79 eV were attributed to the crystal lattice oxygen and chemisorbed oxygen resulted from citrate groups, respectively [48]. Finally, two peaks at 369.17 and 375.39 eV attributing to Ag3d5/2 and Ag3d3/2 confirmed Ag presence (Fig. 2F).

Magnetic properties of $CoFe_2O_4$@Ag nanocomposite and $CoFe_2O_4$ were investigated at 25 °C using a vibrating-sample magnetometer. According to Fig. S4, the magnetization saturation (Ms) values for $CoFe_2O_4$ and $CoFe_2O_4$@Ag nanocomposite were calculated as 52.79 emu g^{-1}, and 41.19 emu g^{-1}, respectively [43]. Owing to non-magnetic mass, the decrease in Ms value was observed. However, the high Ms value having $CoFe_2O_4$@Ag nanocomposite demonstrated that the prepared nanocomposite was easily isolated by an external magnet.

3.3. Characterizations of AuNPs@MoS_2/rGO

Firstly, the XRD method was carried out for determining the crystal structures of rGO, MoS_2/rGO and AuNPs@MoS_2/rGO. According to Fig. S5, two XRD peaks corresponding to 24.68° and 43.19° showed graphite-like structure (002) and (100) of rGO. XRD spectra of MoS_2/rGO and AuNPs@MoS_2/rGO showed the similar patterns attributing to (002), (101), (103) and (110) planes. Three

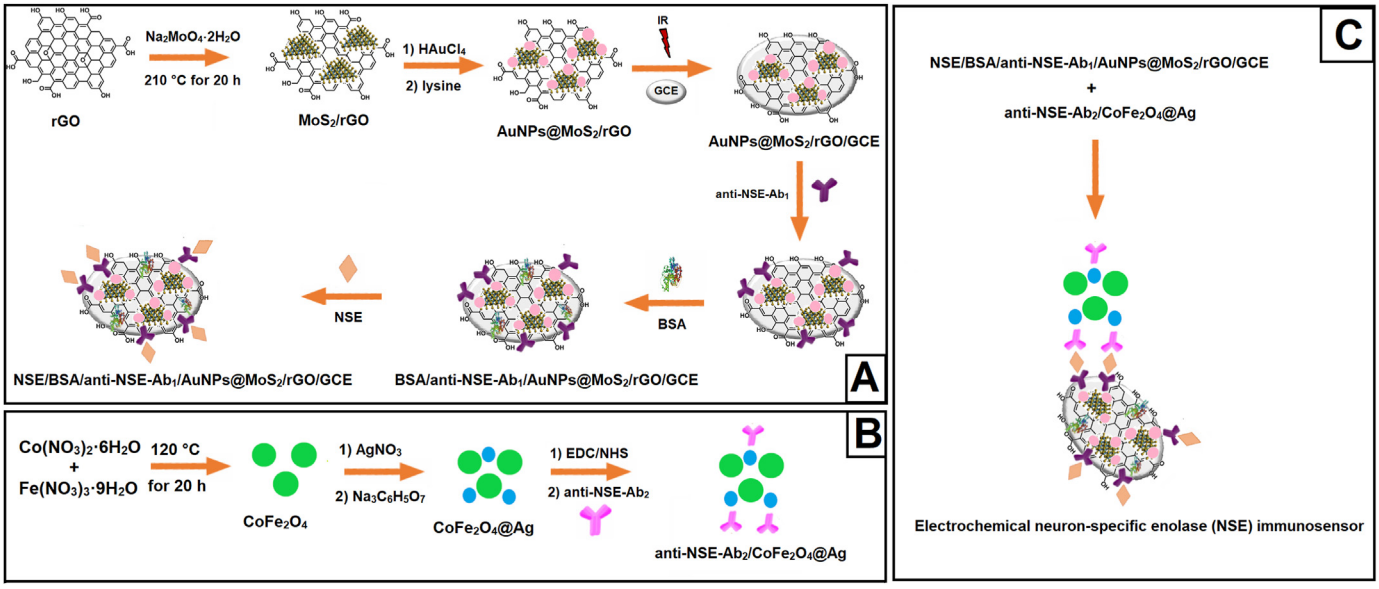

Scheme 1. Schematic representation of the fabrication of electrochemical NSE immunosensor Fig. 1. SEM images of (A) $CoFe_2O_4$, (B) $CoFe_2O_4$@Ag nanocomposite.

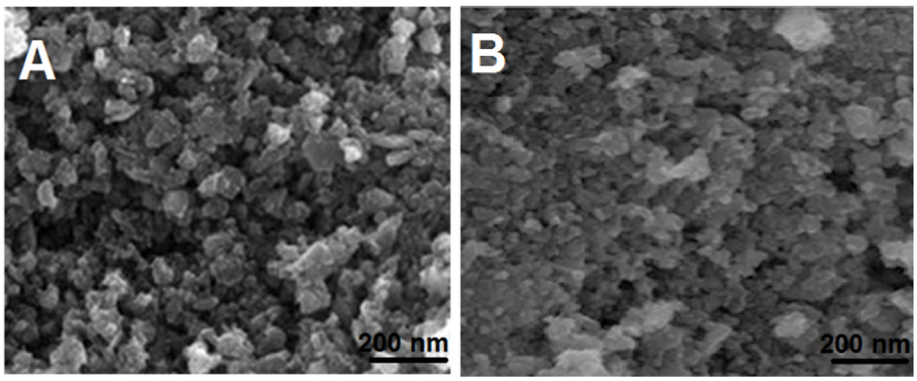

Fig. 1. SEM images of (A) CoFe2O4, (B) CoFe2O4@Ag nanocomposite.

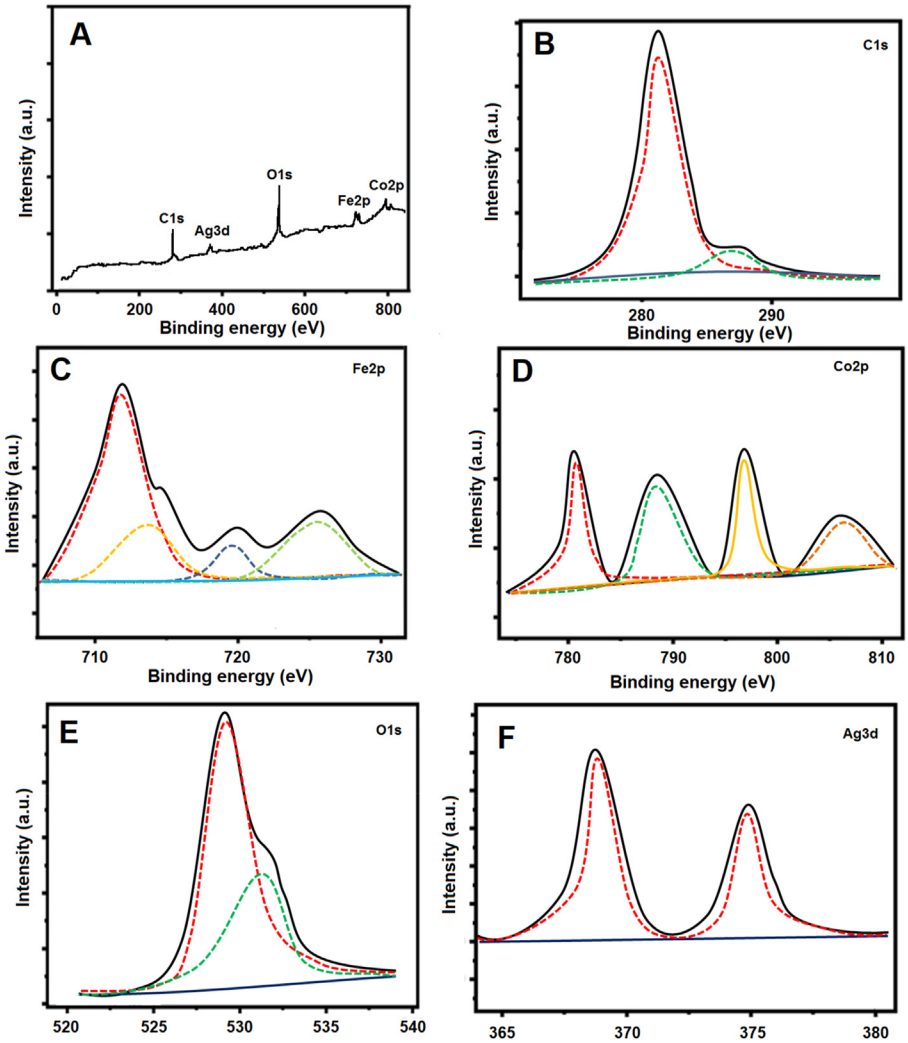

Fig. 2. (A) XPS survey of $CoFe_2O_4$@Ag nanocomposite and high-resolution XPS spectrum of (B) C1s, (C) Fe2p, (D) Co2p, (E) O1s, (F) Ag3d.

peaks at 39.08°, 44.89° and 65.78° were attributed to (111), (200) and (220) planes of Au, confirming AuNPs modification on MoS_2/rGO composite. Afterward, the structures and morphologies of rGO, MoS_2/rGO and AuNPs@MoS_2/rGO were investigated by SEM (Fig. 3). Fig. 3A showed the wrinkle structure of rGO. The typical flower morphology of MoS_2 with an average diameter of 5–8 μm was observed on Fig. 3B. Fig. 3C confirmed rGO coating on MoS2 nanosheets after ultrasonication. Finally, the successful coating of AuNPs on MoS_2/rGO was observed on Fig. 3D. Hence, AuNPs@MoS_2/rGO was used as an electrode platform due to the larger electrochemical surface area providing easy contact between target and electrode surface. In addition, the prepared electrode platform facilitated the electron transfer, thereby boosting the electrochemical sensitivity.

The morphology properties of AuNPs@MoS_2/rGO was also evaluated by TEM (Fig. S6A), confirming the successful coating of AuNPs on MoS2/rGO composite. According to HRTEM images (Fig. S6B and Fig. S6C), the lattice fringes were calculated as 0.60 nm and 0.25 nm, attributing to the interplanar spacing of MoS_2 (002) plane and AuNPs (111) plane, respectively. Therefore, the interplanar spacing values verified the successfully modification of AuNPs on MoS2/rGO composite.

Lastly, the surface composition and the element valence of AuNPs@MoS_2/rGO nanocomposite were investigated by XPS (Fig. S7). Two peaks at 84.18 and 88.25 eV attributing to Au4f7/2 and Au4f5/2, respectively confirmed the presence of AuNPs (Fig. S7A). Two strong XPS peaks at 230.17 eV and 232.69 eV were ascribed to Mo3d5/2 and Mo3d3/2, respectively, and the weak XPS peak at 227.27 eV was related to S2s in MoS_2 (Fig. S7B). According to Fig. S7C, two peaks at 161.83 and 163.93 eV on S2p spectrum were attributed to S2p3/2 and S2p1/2, respectively [49,50]. Furthermore, the strong peak at 285.11 eV and the weak peak at 285.93 eV on the C1s spectrum corresponded to the sp^2 hybridized graphitic carbon (C−C) group and the remained oxygen-containing (C−O) functional groups, respectively (Fig. S7D) [25,51].

3.4. Assessment of the electrochemical performance of the sensor platform and signal amplification

CV and EIS methodologies were carried out to explore the electrochemical features of the as-prepared sensor platform in the presence of 1.0 mM $[Fe(CN)_6]^{3-/4-}$. Initially, an anodic peak at +1.22 V and a cathodic peak at +0.63 V were observed by using bare GCE (curve a of Fig. 4A). After the employment of rGO/GCE (curve b of Fig. 4A), the obvious increment in the electrochemical response was observed thanks to the rGO's good electrochemical activity [52]. When the synthesized MoS_2/rGO/GCE (curve c of Fig. 4A) and AuNPs@MoS_2/rGO/GCE (curve d of Fig. 4A) were applied to 1.0 mM $[Fe(CN)_6]^{3-/4-}$, boosted square wave currents (ISWs) were observed owing to MoS_2/rGO composite's high conductivity [23] and the synergistic effect between AuNPs and MoS_2/rGO composite [25]. In addition, AuNPs's electrical conductivity delivered an enhancement in the sensor signals [53]. The blocking impact of anti-NSE-Ab_1 caused the apparent declines in anodic and cathodic signals, as expected (curve e of Fig. 4A). Moreover, the immobilizations of BSA (curve f of Fig. 4A) and antigen NSE (curve g of Fig. 4A) on anti-NSE-Ab_1/AuNPs@MoS_2/rGO/GCE, respectively, resulted in more electron transfer blocking effect. Thus, according to curve f and g of Fig. 4A, the immobilizations of BSA and antigen NSE were successfully performed. Lastly, the further decreases on anodic and cathodic signals were observed by the final immunosensor (curve h of Fig. 4A).

In order to verify CV results, EIS measurements were subsequently implemented (Fig. 4B). The charge transfer resistances were determined to be 260 Ω for bare GCE (curve a), 250 Ω for rGO/GCE (curve b), 230 Ω for MoS_2/rGO/GCE (curve c), 180 Ω for AuNPs@MoS_2/rGO/GCE (curve d), 200 Ω for anti-NSE-Ab_1/AuNPs@MoS_2/rGO/GCE (curve e), 210 Ω for BSA/anti-NSE-Ab_1/AuNPs@MoS_2/rGO/GCE (curve f), 220 Ω for NSE/BSA/anti-NSE-Ab_1/AuNPs@MoS_2/rGO/GCE (curve g) and 225 Ω for the final immunosensor (curve h). Hence, the findings highlighted the fact that CV and EIS results were in good harmony.

Lastly, for the gradual electrochemical characterization of the developed signal amplification (Fig. 4C), two distinct electrochemical NSE immunosensors containing 0.20 pg mL^{-1} antigen NSE were prepared by using different signal amplifications including anti-NSE-Ab_2/$CoFe_2O_4$ (curve b of Fig. 4C), and anti-NSE-Ab_2/$CoFe_2O_4$@Ag (curve c of Fig. 4C) at the immune reaction period of 25 min. ISWs were recorded in presence of 1.0 mM H_2O_2. Due to biocompatibility of $CoFe_2O_4$ and its composites [27] and the strong covalent bond formation during the preparation of anti-NSE-Ab_2/$CoFe_2O_4$@Ag, anti-NSE-Ab_2/$CoFe_2O_4$@Ag produced the greatest electrochemical immunosensor signals when compared to anti-NSE-Ab_2/$CoFe_2O_4$ (Fig. 4C).

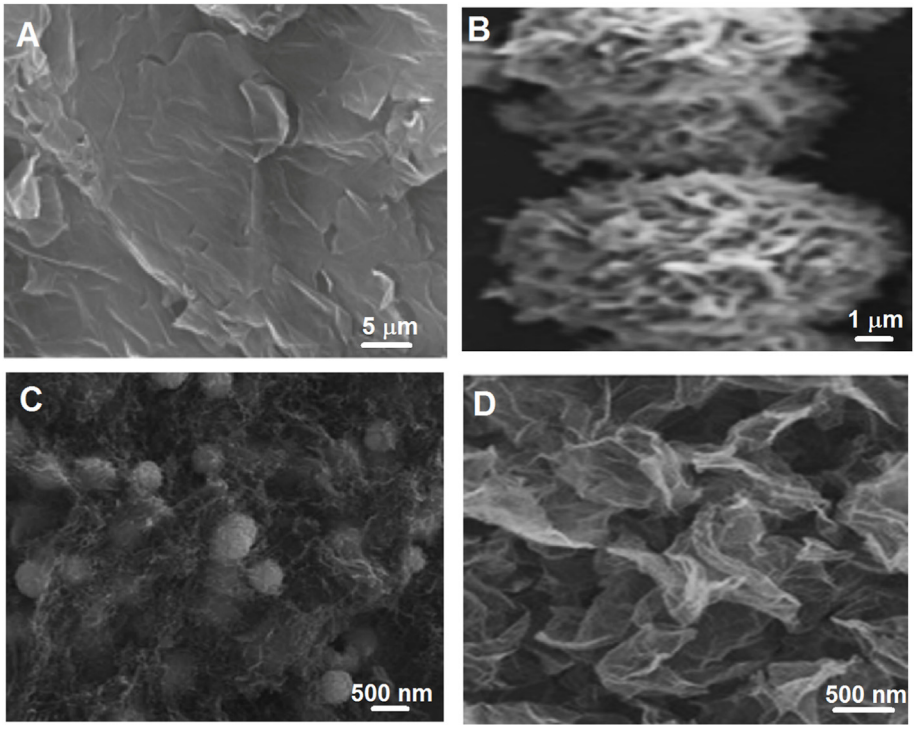

Fig. 3. SEM images of (A) rGO, (B) MoS_2, (C) MoS_2/rGO, (D) AuNPs@MoS_2/rGO

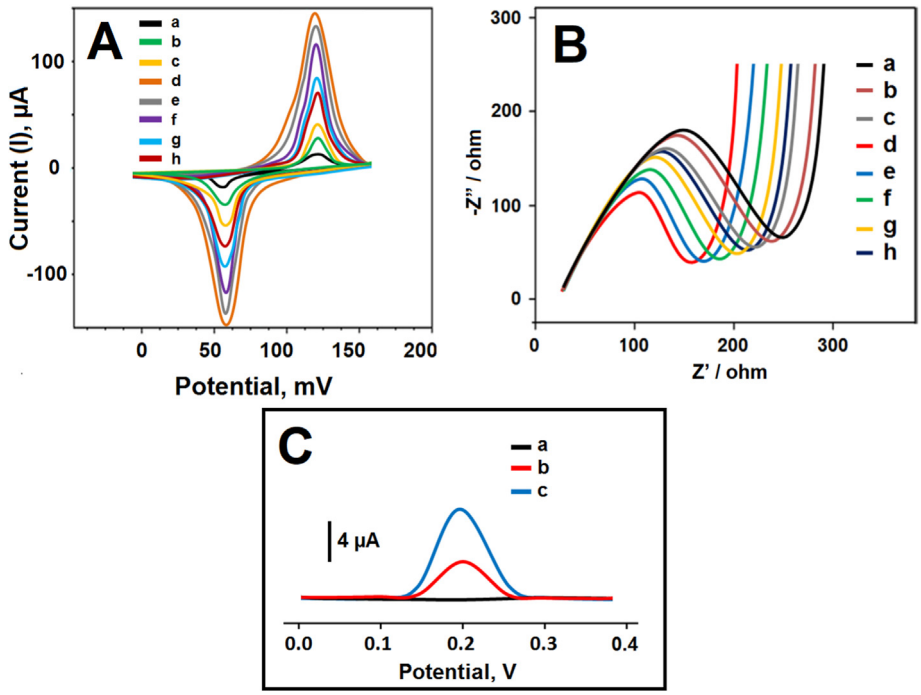

Fig. 4. (A) Cyclic voltammograms, (B) EIS reponses at (a) bare GCE, (b) rGO/GCE, (c) MoS_2/rGO/GCE, (d) AuNPs@MoS_2/rGO/GCE, (e) anti-NSE-Ab_1/AuNPs@MoS_2/rGO/GCE, (f) BSA/anti-NSE-Ab_1/AuNPs@MoS_2/rGO/GCE, (g) NSE/BSA/anti-NSE-Ab_1/AuNPs@MoS_2/rGO/GCE, (h) the final immunosensor including anti-NSE-Ab_1, antigen NSE and anti-NSE-Ab_2 (scan rate of 100 mV s^{-1}) in 1.0 mM $[Fe(CN)_6]^{3-}$ containing 0.1 M KCl and (C) SWV responses of the developed immunosensors incubated with 0.20 pg mL^{-1} antigen NSE using anti-NSE-Ab_2/$CoFe_2O_4$ (curve b) and anti-NSE-Ab_2/$CoFe_2O_4$@Ag (curve c) in absence of H_2O_2 (curve a) and in presence of 1.0 mM H_2O_2 (Parameters are frequency of 100 Hz, pulse amplitude of 25 mV, scan increment of 5 mV for SWV measurements).

3.5. Optimization for electrochemical measurements

The influences of solution pH, the period of immunological reaction, H_2O_2, and the concentration of anti-NSE-Ab_2/$CoFe_2O_4$@Ag solution were examined in detail in optimization studies. (Fig. S8).

3.6. Linearity range

The acquired calibration equation [I (µA) = 23.631C_{NSE} (pg mL^{-1})] + 0.2393,(R^2 = 0.9991) by increasing antigen NSE concentrations and differential pulse signals was depicted in Fig. 5. LOQ, and LOD were found to be 0.01 pg mL^{-1}, and 3.00 fg mL^{-1}, respectively, by equations (1) and (2):

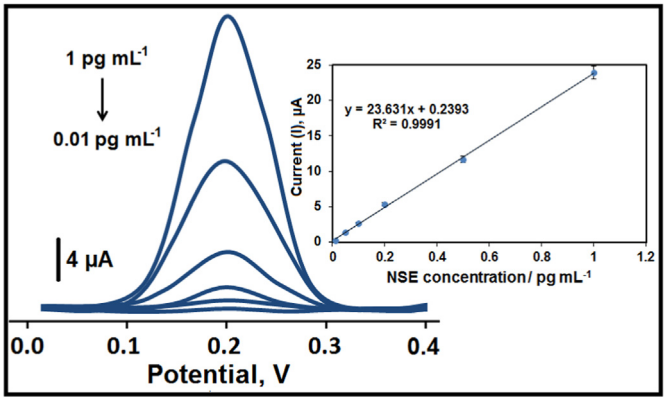

Fig. 5. Concentration effect (from 0.01 to 1.0 pg mL^{-1} NSE) on immunosensor current (I) signals, Inset: Calibration curve for electrochemical NSE immunosensor (Potential range is +0.0/+0.4 V; Parameters are frequency of 100 Hz, pulse amplitude of 25 mV, scan increment of 5 mV for SWV measurements) (n = 6).

$$LOQ = 10.0\ S / m \quad (1)$$

$$LOD = 3.3\ S / m \quad (2)$$

Where S is the standard deviation of the intercept and m is the slope of the regression line. Table 1 summarized how the constructed electrochemical NSE immunosensor outperformed in comparison to the existing approaches in terms of sensitivity and linearity. Firstly, the sensitive electrochemical NSE analysis with LOD of 3.00 fg mL^{-1} was successfully completed in comparison with the other techniques. In addition, the offered synthesis approach of $CoFe_2O_4$@Ag and AuNPs@MoS_2/rGO nanocomposites during immunosensor development was especially time-saving and environmentally friendly. Lastly, the prepared immunosensor illustrated excellent analytical performance metrics towards NSE determination.

3.7. Recovery

For recovery experiments, four different plasma samples were prepared (Plasma sample1, Plasma sample2, Plasma sample3 and Plasma sample4). The contents of solutions were presented in detail on Supplementary Data. Table S1 showed the recovery values of NSE in the presence of 0.1 M PBS (pH 7.0) including 1.0 mM H_2O_2, which were obtained by Equation (3).

$$Recovery = Found\ NSE,\ pg\ mL^{-1} / Real\ NSE,\ pg\ mL^{-1} \quad (3)$$

According to Table S1 of recovery experiments, the close to 100.00% values confirmed the high accuracy of the electrochemical immunosensor, providing the successful NSE determination without interference effect. Moreover, standard addition method was conducted to experimental samples and I (µA) = 23.601C_{NSE}

Table 1
The comparison of linear range and the LOD metrics for constructed electrochemical NSE immunosensor with other existing approaches.

Material/Method	Linear Range	LOD	Ref.
SERS	0.50 ng mL^{-1} – 0.1 mg mL^{-1}	0.86 ng mL^{-1}	[54]
Ag@Ti_3C_2-MXene	0.0001–1500 ng mL^{-1}	0.05 pg mL^{-1}	[55]
Au–MoS_2/MOF	1.00 pg mL^{-1} – 100.0 ng mL^{-1}	0.37 pg mL^{-1}	[56]
SERS	0.0001–1000 ng mL^{-1}	0.01 pg mL^{-1}	[57]
Au/Fc@Cu_xO SPs	500.00 fg mL^{-1} – 100.0 ng mL^{-1}	25.70 fg mL^{-1}	[58]
Au/Cu_xO@CeO_2	50.00 fg mL^{-1} – 100.0 ng mL^{-1}	31.30 fg mL^{-1}	[59]
ECL-RET	0.20 pg mL^{-1} – 20.0 ng mL^{-1}	79.0 fg mL^{-1}	[60]
MnO_2 UNs/Au@Pd^Pt NCs	10.00 fg mL^{-1} – 100.0 ng mL^{-1}	4.17 fg mL^{-1}	[61]
EIS	10.00 fg mL^{-1} – 2.0 ng mL^{-1}	7.10 fg mL^{-1}	[62]
Sandwich type immunosensor	***0.01 – 1.00 pg mL^{-1}***	**3.00 fg mL^{-1}**	***This study***

(pg mL^{-1}) + 10.0379, R^2 = 0.9996 was obtained as calibration equation. Therefore, the close slope values between direct calibration (inset of Fig. 5) and standard addition methods verified the high selective NSE determination.

3.8. Assessment of the selectivity, stability, repeatability and reusability of the fabricated electrochemical NSE immunosensor

Five electrochemical NSE immunosensors were designed to illustrate the enhanced selectivity of electrochemical immunosensors. With this regard, the fabricated five electrochemical NSE immunosensors were applied to the prepared protein solutions such as (i) 200.00 pg mL^{-1} PSA + 200.00 pg mL^{-1} BSA + 200.00 pg mL^{-1} cTnI + 200.00 pg mL^{-1} CEA, (ii) 0.200 pg mL^{-1} NSE + 200.00 pg mL^{-1} PSA, (iii) 0.200 pg mL^{-1} NSE + 200.00 pg mL^{-1} BSA, (iv) 0.200 pg mL^{-1} NSE +200.00 pg mL^{-1} cTnI, (v) 0.200 pg mL^{-1} NSE + 200.00 pg mL^{-1} CEA in presence of 1.0 mM H_2O_2 solution. Fig. S9A verified that the other proteins (PSA, BSA, cTnI and CEA) did not affect the high selective electrochemical performance for NSE determination. The exceptional stability of the electrochemical immunosensor was also demonstrated by the acquisition of differential pulse signals (Fig. S9B) over a seven-week period. According to Fig. S9B, the obtained current (I) signal at the end of the seventh week was determined *ca*.98.39% of the end of the first week, confirming the superior stability of the fabricated electrochemical NSE immunosensor. For repeatability test, 15 different electrochemical NSE immunosensors were constructed according to the provided procedure in section of 2.4, 2.5 and 2.6. The relative standard deviation (RSD) of the obtained ISWs was calculated as to be 0.48, revealing the excellent reliability for the protocol of immunosensor fabrication.

Lastly, reusability of electrochemical NSE immunosensor was finally performed by following the current (I) signals belonging to only one prepared NSE immunosensor during its 30 times usages. RSD value as 0.69% was obtained, suggesting a high degree of reusability.

4. Conclusions

The monitoring of the NSE protein as a diagnostic for small cell lung cancer is crucial since it can foreshadow early metastasis. Herein, a facile, selective, and sensitive electrochemical immunosensor was fabricated based on GCE modified AuNPs@MoS_2/rGO to immobilize a specific anti-NSE capture antibody for antigen NSE recognition and $CoFe_2O_4$@Ag nanocomposite as signal amplification. The immunosensor offered a highly sensitive determination of antigen NSE with a wide linearity (from 0.01 to 1.00 pg mL^{-1}), and a LOD of 3.00 fg mL^{-1}, demonstrating the utility of the immunosensor in the early determination of lung cancer at the onset stage. Furthermore, in the presence of other interfering proteins, the immunosensor revealed a high binding affinity for antigen NSE. In a nutshell, this research could pave the ground for the emergence of a highly selective and sensitive electrochemical immunosensor for the early determination of small cell lung cancer.

CRediT authorship contribution statement

Ceren Karaman: Conceptualization, Methodology, Writing – review & editing. **Ömer Saltuk Bölükbaşı:** Data curation, Visualization, Investigation. **Bahar Bankoğlu Yola:** Data curation, Visualization, Investigation. **Onur Karaman:** Writing – original draft, Visualization. **Necip Atar:** Writing – original draft, Visualization, Investigation. **Mehmet Lütfi Yola:** Supervision, Conceptualization, Writing – review & editing.

Declaration of competing interest

The authors declare that they have no known competing financial interests or personal relationships that could have appeared to influence the work reported in this paper.

Acknowledgement

Mehmet Lütfi YOLA would like to thank Turkish Academy of Sciences for their invaluable support in respect to The Young Scientists Award Programme, TÜBA-GEBIP (2019).

Appendix A. Supplementary data

Supplementary data to this article can be found online at https://doi.org/10.1016/j.aca.2022.339609.

References

[1] C.M. Rudin, E. Brambilla, C. Faivre-Finn, J. Sage, Small-cell lung cancer, Nat. Rev. Dis. Prim. 7 (2021) 1–20.
[2] A.M.C. Dingemans, M. Fruh, A. Ardizzoni, B. Besse, C. Faivre-Finn, L.E. Hendriks, S. Lantuejoul, S. Peters, N. Reguart, C.M. Rudin, D. De Ruysscher, P.E. Van Schil, J. Vansteenkiste, M. Reck, E.G. Comm, Small-cell lung cancer: ESMO Clinical Practice Guidelines for diagnosis, treatment and follow-up, Ann. Oncol. 32 (2021) 839–853.
[3] D.M. Jackman, B.E. Johnson, Small-cell lung cancer, Lancet 366 (2005) 1385–1396.
[4] S. Dolati, J. Soleymani, S.K. Shakouri, A. Mobed, The trends in nanomaterial-based biosensors for detecting critical biomarkers in stroke, Clin. Chim. Acta 514 (2021) 107–121.
[5] X. Wang, Y.Y. Wang, X.X. Ye, T. Wu, H.P. Deng, P. Wu, C.Y. Li, Sensing platform for neuron specific enolase based on molecularly imprinted polymerized ionic liquids in between gold nanoarrays, Biosens. Bioelectron. 99 (2018) 34–39.
[6] T.X. Yu, W. Cheng, Q. Li, C.H. Luo, L. Yan, D.C. Zhang, Y.B. Yin, S.J. Ding, H.X. Ju, Electrochemical immunosensor for competitive detection of neuron specific enolase using functional carbon nanotubes and gold nanoprobe, Talanta 93 (2012) 433–438.
[7] L.S. Zhao, S.Y. Xu, G. Fjaertoft, K. Pauksen, L. Hakansson, P. Venge, An enzyme-linked immunosorbent assay for human carcinoembryonic antigen-related cell adhesion molecule 8, a biological marker of granulocyte activities

in vivo, J. Immunol. Methods 293 (2004) 207–214.
[8] T. Tagi, T. Matsui, S. Kikuchi, S. Hoshi, T. Ochiai, Y. Kokuba, Y. Kinoshita-Ida, F. Kisumi-Hayashi, K. Morimoto, T. Imai, I. Imoto, J. Inazawa, E. Otsuji, Dermokine as a novel biomarker for early-stage colorectal cancer, J. Gastroenterol. 45 (2010) 1201–1211.
[9] S.W. Oh, Y.M. Kim, H.J. Kim, S.J. Kim, J.S. Cho, E.Y. Choi, Point-of-care fluorescence immunoassay for prostate specific antigen, Clin. Chim. Acta 406 (2009) 18–22.
[10] C. Karaman, O. Karaman, B.B. Yola, I. Ulker, N. Atar, M.L. Yola, A novel electrochemical aflatoxin B1 immunosensor based on gold nanoparticle-decorated porous graphene nanoribbon and Ag nanocube-incorporated MoS2 nanosheets, New J. Chem. 45 (2021) 11222–11233.
[11] O. Karaman, N. Ozcan, C. Karaman, B.B. Yola, N. Atar, M.L. Yola, Electrochemical cardiac troponin I immunosensor based on nitrogen and boron-doped graphene quantum dots electrode platform and Ce-doped SnO2/SnS2 signal amplification, Mater. Today Chem. 23 (2022) 100666.
[12] Y. Chen, P.X. Yuan, A.J. Wang, X.L. Luo, Y.D. Xue, L. Zhang, J.J. Feng, A novel electrochemical immunosensor for highly sensitive detection of prostate-specific antigen using 3D open-structured PtCu nanoframes for signal amplification, Biosens. Bioelectron. 126 (2019) 187–192.
[13] X. Zhou, Q.L. Pu, H.Y. Yu, Y. Peng, J.J. Li, Y.J. Yang, H.J. Chen, Y.G. Weng, G.M. Xie, An electrochemical biosensor based on hemin/G-quadruplex DNAzyme and PdRu/Pt heterostructures as signal amplifier for circulating tumor cells detection, J. Colloid Interface Sci. 599 (2021) 752–761.
[14] C.Y. Tang, P. Wang, K.W. Zhou, J. Ren, S.J. Wang, F. Tang, Y.Y. Li, Q. Liu, L. Xue, Electrochemical immunosensor based on hollow porous Pt skin AgPt alloy/NGR as a dual signal amplification strategy for sensitive detection of Neuron-specific enolase, Biosens. Bioelectron. 197 (2022) 113779.
[15] H. Karimi-Maleh, F. Karimi, L. Fu, A.L. Sanati, M. Alizadeh, C. Karaman, Y. Orooji, Cyanazine herbicide monitoring as a hazardous substance by a DNA nanostructure biosensor, J. Hazard Mater. 423 (2022) 127058.
[16] M. Soleimani, J.B. Ghasemi, G.M. Ziarani, H. Karimi-Maleh, A. Badiei, Photocatalytic degradation of organic pollutants, viral and bacterial pathogens using titania nanoparticles, Inorg. Chem. Commun. 130 (2021) 108688.
[17] C. Karaman, O. Karaman, N. Atar, M.L. Yola, Sustainable electrode material for high-energy supercapacitor: biomass-derived graphene-like porous carbon with three-dimensional hierarchically ordered ion highways, Phys. Chem. Chem. Phys. 23 (2021) 12807–12821.
[18] E. Bayram, C. Karaman, Z. Kuru, O. Karaman, Electrosorptive disinfection of Escherichia coli (E. coli) aqueous solutions by activated carbon monolith electrodes, Water Supply 21 (2021) 157–165.
[19] C. Karaman, E. Bayram, O. Karaman, Z. Aktas, Preparation of high surface area nitrogen doped graphene for the assessment of morphologic properties and nitrogen content impacts on supercapacitors, J. Electroanal. Chem. 868 (2020) 114197.
[20] Y. Haldorai, J.Y. Kim, A.T.E. Vilian, N.S. Heo, Y.S. Huh, Y.K. Han, An enzyme-free electrochemical sensor based on reduced graphene oxide/Co3O4 nanospindle composite for sensitive detection of nitrite, Sensor. Actuator. B Chem. 227 (2016) 92–99.
[21] Y.J. Han, X.J. Su, L.F. Fan, Z.G. Liu, Y.J. Guo, Electrochemical aptasensor for sensitive detection of Cardiac troponin I based on CuNWs/MoS2/rGO nanocomposite, Microchem. J. 169 (2021) 106598.
[22] J.V. Piovesan, E.R. Santana, A. Spinelli, Reduced graphene oxide/gold nanoparticles nanocomposite-modified glassy carbon electrode for determination of endocrine disruptor methylparaben, J. Electroanal. Chem. 813 (2018) 163–170.
[23] N.I. Ikhsan, P. Rameshkumar, A. Pandikumar, M.M. Shahid, N.M. Huang, S.V. Kumar, H.N. Lim, Facile synthesis of graphene oxide-silver nanocomposite and its modified electrode for enhanced electrochemical detection of nitrite ions, Talanta 144 (2015) 908–914.
[24] F.L. Zhang, Z.G. Liu, Y.J. Han, L.F. Fan, Y.J. Guo, Sandwich electrochemical carcinoembryonic antigen aptasensor based on signal amplification of polydopamine functionalized graphene conjugate Pd-Pt nanodendrites, Bioelectrochemistry 142 (2021) 107947.
[25] Y. Yang, Q. Lei, J. Li, C. Hong, Z.T. Zhao, H.Y. Xu, J. Hu, Synthesis and enhanced electrochemical properties of AuNPs@MoS2/rGO hybrid structures for highly sensitive nitrite detection, Microchem. J. 172 (2022) 106904.
[26] F. Moreira, E.R. Santana, A. Spinelli, Ionic liquid-supported magnetite nanoparticles as electrode modifier materials for estrogens sensing, Sci. Rep.-Uk 10 (2020) 1–11.
[27] S.Y. Srinivasan, K.M. Paknikar, D. Bodas, V. Gajbhiye, Applications of cobalt ferrite nanoparticles in biomedical nanotechnology, Nanomedicine-Uk 13 (2018) 1221–1238.
[28] L. Tian, J.X. Qi, K. Qian, O. Oderinde, Q.Y. Liu, C. Yao, W. Song, Y.H. Wang, Copper (II) oxide nanozyme based electrochemical cytosensor for high sensitive detection of circulating tumor cells in breast cancer, J. Electroanal. Chem. 812 (2018) 1–9.
[29] M. Haddaoui, C. Sola, N. Raouafi, H. Korri-Youssoufi, E-DNA detection of rpoB gene resistance in Mycobacterium tuberculosis in real samples using Fe3O4/polypyrrole nanocomposite, Biosens. Bioelectron. 128 (2019) 76–82.
[30] Y. Guo, Y.C. Tao, X.W. Ma, J. Jin, S.S. Wen, W. Ji, W. Song, B. Zhao, Y. Ozaki, A dual colorimetric and SERS detection of Hg2+ based on the stimulus of intrinsic oxidase-like catalytic activity of Ag-CoFe2O4/reduced graphene oxide nanocomposites, Chem. Eng. J. 350 (2018) 120–130.
[31] A. Sengupta, R. Rao, D. Bahadur, Zn2+-Silica modified cobalt ferrite magnetic nanostructured composite for efficient adsorption of cationic pollutants from water, Acs Sustain. Chem. Eng. 5 (2017) 1280–1286.
[32] C.Z. Fan, K. Li, J.X. Li, D.W. Ying, Y.L. Wang, J.P. Jia, Comparative and competitive adsorption of Pb(II) and Cu(II) using tetraethylenepentamine modified chitosan/CoFe2O4 particles, J. Hazard Mater. 326 (2017) 211–220.
[33] Y. He, Y. Wang, X. Yang, S.B. Xie, R. Yuan, Y.Q. Chai, Metal organic frameworks combining CoFe2O4 magnetic nanoparticles as highly efficient SERS sensing platform for ultrasensitive detection of N-terminal pro-brain natriuretic peptide, Acs Appl. Mater. Interfaces 8 (2016) 7683–7690.
[34] M.L. Yola, T. Eren, N. Atar, A novel and sensitive electrochemical DNA biosensor based on Fe@Au nanoparticles decorated graphene oxide, Electrochim. Acta 125 (2014) 38–47.
[35] M.L. Yola, N. Atar, M.S. Qureshi, Z. Ustundag, A.O. Solak, Electrochemically grafted etodolac film on glassy carbon for Pb(II) determination, Sensor. Actuator. B Chem. 171 (2012) 1207–1215.
[36] G.Q. Zhou, W.Y. Wang, Synthesis of silver nanoparticles and their anti-proliferation against human lung cancer cells in vitro, Orient. J. Chem. 28 (2012) 651–655.
[37] F. Vajhadin, M. Mazloum-Ardakani, M. Shahidi, S.M. Moshtaghioun, F. Haghiralsadat, A. Ebadi, A. Amini, MXene-based cytosensor for the detection of HER2-positive cancer cells using CoFe2O4@Ag magnetic nanohybrids conjugated to the HB5 aptamer, Biosens. Bioelectron. 195 (2022) 113626.
[38] B. Jeong, R. Akter, O.H. Han, C.K. Rhee, M.A. Rahman, Increased electrocatalyzed performance through dendrimer-encapsulated gold nanoparticles and carbon nanotube-assisted multiple bienzymatic labels: highly sensitive electrochemical immunosensor for protein detection, Anal. Chem. 85 (2013) 1784–1791.
[39] M.L. Yola, N. Atar, Development of cardiac troponin-I biosensor based on boron nitride quantum dots including molecularly imprinted polymer, Biosens. Bioelectron. 126 (2019) 418–424.
[40] J.V. Piovesan, C.A. de Lima, E.R. Santana, A. Spinelli, Voltammetric determination of condensed tannins with a glassy carbon electrode chemically modified with gold nanoparticles stabilized in carboxymethylcellulose, Sensor. Actuator. B Chem. 240 (2017) 838–847.
[41] M.L. Yola, N. Atar, Novel voltammetric tumor necrosis factor-alpha (TNF-alpha) immunosensor based on gold nanoparticles involved in thiol-functionalized multi-walled carbon nanotubes and bimetallic Ni/Cu-MOFs, Anal. Bioanal. Chem. 413 (2021) 2481–2492.
[42] H. Medetalibeyoglu, M. Beytur, O. Akyildirim, N. Atar, M.L. Yola, Validated electrochemical immunosensor for ultra -sensitive procalcitonin detection: carbon electrode modified with gold nanoparticles functionalized sulfur doped MXene as sensor platform and carboxylated graphitic carbon nitride as signal amplification, Sensor. Actuator. B Chem. 319 (2020) 128195.
[43] J.M.N. dos Santos, C.R. Pereira, L.A.A. Pinto, T. Frantz, E.C. Lima, E.L. Foletto, G.L. Dotto, Synthesis of a novel CoFe2O4/chitosan magnetic composite for fast adsorption of indigotine blue dye, Carbohydr. Polym. 217 (2019) 6–14.
[44] A.A.G. El-Shahawy, F.I.A. El-Ela, N.A. Mohamed, Z.E. Eldine, W.M.A. El Rouby, Synthesis and evaluation of layered double hydroxide/doxycycline and cobalt ferrite/chitosan nanohybrid efficacy on gram positive and gram negative bacteria, Mater. Sci. Eng. C-Mater. 91 (2018) 361–371.
[45] S. Nappini, E. Magnano, F. Bondino, I. Pis, A. Barla, E. Fantechi, F. Pineider, C. Sangregorio, L. Vaccari, L. Venturelli, P. Baglioni, Surface charge and coating of CoFe2O4 nanoparticles: evidence of preserved magnetic and electronic properties, J. Phys. Chem. C 119 (2015) 25529–25541.
[46] M. Haghshenas, M. Mazloum-Ardakani, Z. Alizadeh, F. Vajhadin, H. Naeimi, A sensing platform using Ag/Pt core-shell nanostructures supported on multiwalled carbon nanotubes to detect hydroxyurea, Electroanalysis 32 (2020) 2137–2145.
[47] F.B. Zhao, Y.C. Zou, X.J. Lv, H.W. Liang, Q. Jia, W.K. Ning, Synthesis of CoFe2O4-zeolite materials and application to the adsorption of gallium and indium, J. Chem. Eng. Data 60 (2015) 1338–1344.
[48] W.P. Wang, H. Yang, T. Xian, J.L. Jiang, XPS and magnetic properties of CoFe2O4 nanoparticles synthesized by a polyacrylamide gel route, Mater. Trans. 53 (2012) 1586–1589.
[49] Y.X. Chen, X. Wu, K.J. Huang, A sandwich-type electrochemical biosensing platform for microRNA-21 detection using carbon sphere-MoS2 and catalyzed hairpin assembly for signal amplification, Sensor. Actuator. B Chem. 270 (2018) 179–186.
[50] C.H. Lin, C.H. Tsai, F.G. Tseng, C.C.M. Ma, H.C. Wu, C.K. Hsieh, Three-dimensional vertically aligned hybrid nanoarchitecture of two-dimensional molybdenum disulfide nanosheets anchored on directly grown one-dimensional carbon nanotubes for use as a counter electrode in dye-sensitized solar cells, J. Alloys Compd. 692 (2017) 941–949.
[51] S.H. Liu, L.X. Yang, S.H. Xu, S.L. Luo, Q.Y. Cai, Photocatalytic activities of C-N-doped TiO2 nanotube array/carbon nanorod composite, Electrochem. Commun. 11 (2009) 1748–1751.
[52] Z. Shi, G. Sun, R. Yuan, W. Chen, Z. Wang, L. Zhang, K. Zhan, M. Zhu, J. Yang, B. Zhao, Scalable fabrication of NiCo2O4/reduced graphene oxide composites by ultrasonic spray as binder-free electrodes for supercapacitors with ultra-long lifetime, J. Mater. Sci. Technol. 99 (2022) 260–269.
[53] P. Rodriguez, D. Plana, D.J. Fermin, M.T.M. Koper, New insights into the catalytic activity of gold nanoparticles for CO oxidation in electrochemical media, J. Catal. 311 (2014) 182–189.
[54] X.F. Gao, P. Zheng, S. Kasani, S. Wu, F. Yang, S. Lewis, S. Nayeem, E.B. Engler-Chiurazzi, J.G. Wigginton, J.W. Simpkins, N.Q. Wu, Paper-based surface-

enhanced Raman scattering lateral flow strip for detection of neuron-specific enolase in blood plasma, Anal. Chem. 89 (2017) 10104−10110.
[55] A. Kalkal, S. Kadian, S. Kumar, G. Manik, P. Sen, S. Kumar, G. Packirisamy, Ti3C2-MXene decorated with nanostructured silver as a dual-energy acceptor for the fluorometric neuron specific enolase detection, Biosens. Bioelectron. 195 (2022) 113620.
[56] H. Dong, S.H. Liu, Q. Liu, Y.Y. Li, Y.Y. Li, Z.D. Zhao, A dual-signal output electrochemical immunosensor based on Au-MoS2/MOF catalytic cycle amplification strategy for neuron-specific enolase ultrasensitive detection, Biosens. Bioelectron. 195 (2022) 113648.
[57] Y.A. Song, J.Y. Sun, S.J. Zhao, F. Gao, H. Yuan, B.L. Sun, B.J. Wang, Y. Wang, Based lateral flow immunosensor for ultrasensitive and selective surface-enhanced Raman spectroscopy stroke biomarkers detection, Appl. Surf. Sci. 571 (2022) 151153.
[58] X.D. Yu, Y.Y. Li, Y.Y. Li, S.H. Liu, Z.L. Wu, H. Dong, Z. Xu, X.J. Li, Q. Liu, An electrochemical amplification strategy based on the ferrocene functionalized cuprous oxide superparticles for the detection of NSE, Talanta 236 (2022) 122865.
[59] X.D. Yu, X.J. Li, S. Zhang, Y.L. Jia, Z. Xu, X.Y. Li, Z.W. Chen, Y.Y. Li, Ultrasensitive electrochemical detection of neuron-specific enolase based on spiny core-shell Au/CuxO@CeO2 nanocubes, Bioelectrochemistry 138 (2021) 107693.
[60] G.C. Mo, X.M. He, D.M. Qin, X.H. Jiang, X.F. Zheng, B.Y. Deng, A potential-resolved electrochemiluminescence resonance energy transfer strategy for the simultaneous detection of neuron-specific enolase and the cytokeratin 19 fragment, Analyst 146 (2021) 1334−1339.
[61] E.H. Ma, P. Wang, Q.S. Yang, H.X. Yu, F.B. Pei, Y.T. Zheng, Q. Liu, Y.H. Dung, Y.Y. Li, Electrochemical immunosensors for sensitive detection of neuron-specific enolase based on small-size trimetallic Au@PdPt nanocubes functionalized on ultrathin MnO2 nanosheets as signal labels, ACS Biomater. Sci. Eng. 6 (2020) 1418−1427.
[62] Y. Li, C.B. Wang, Z.Z. Li, M.H. Wang, L.H. He, Z.H. Zhang, Zirconium-porphyrin complex as novel nanocarrier for label-free impedimetric biosensing neuron-specific enolase, Sensor. Actuator. B Chem. 314 (2020) 128090.